PCCP

PAPER

View Article Online
View Journal | View Issue

Cite this: *Phys. Chem. Chem. Phys.*, 2023, **25**, 11839

Tuning of the height of energy barrier between locally-excited and charge transfer states by altering the fusing position of *o*-carborane in phenylnaphthalene†

Junki Ochi, Takumi Yanagihara, Kazuo Tanaka * and Yoshiki Chujo

Received 21st January 2023,
Accepted 27th March 2023

DOI: 10.1039/d3cp00334e

rsc.li/pccp

We synthesized two types of the regioisomers fused by a phenylnaphthalene ring with variable connection points to the *o*-carborane scaffold. In this paper, we describe their photoluminescence (PL) properties and detailed photochemical mechanisms. According to the series of optical measurements, interestingly, they showed different PL characters in terms of wavelength and the dual-emission character despite that they have the common aromatic unit. Variable-temperature PL measurements and quantum chemical calculations suggested that the substitution position of aryl groups to *o*-carborane plays an important role in determining the energy barrier to the intramolecular charge-transfer (ICT) state at the S_1 state. Finally, it is revealed that the relative position of the C–C bond of *o*-carborane and the aryl center should be responsible for the photophysical events of aryl-*o*-carboranes.

Introduction

Boron atoms can form various types of cluster compounds constructed by three-center two-electron bonds.[1,2] Among them, *o*-carborane (1,2-dicarba-*closo*-dodecaborane) has been widely investigated as heat-resistant materials,[3] medicinal reagents,[4] and photoluminescent compounds[5] because of its high stability and wide modifiability. One unique property of *o*-carborane is flexibility of the C_{cage}–C_{cage} distance (C_{cage} represents carbon in *o*-carborane) which can be varied in response to the external environment alteration. For example, it is theoretically and experimentally proved that electron-donating groups on the C_{cage} atom elongate the C_{cage}–C_{cage} distance by a back-donation effect.[6,7] More drastically, *o*-carborane dianion possessing two cationic groups on the C_{cage} atom shows more than 1 Å longer C_{cage}–C_{cage} distance from the neutral one.[8–10] Such a flexible character has recently been utilized as uranium capture/release switching triggered by a redox manipulation.[11]

The flexible C_{cage}–C_{cage} character also plays a critical role in a photoluminescence (PL) process. In general, aryl-substituted *o*-carboranes form an intramolecular charge transfer (ICT) state at the S_1 state, showing highly efficient solid-state emission.[5] To date, many reports have described that those compounds show significant structural relaxation around the C_{cage}–C_{cage} bond after photoexcitation.[12–21] Typically, quantum chemical calculations indicate that around 1.66 Å C_{cage}–C_{cage} distance at the S_0 state is elongated to near 2.40 Å at the S_1 state. This unique structural change inspired us to synthesize and investigate the C_{cage}–B_{cage} fused *o*-carboranes by a biphenyl skeleton.[14] The ring-fused structure enabled a highly rigid structure except for the C_{cage}–C_{cage} bond, realizing the targeted investigation of the C_{cage}–C_{cage} elongation. Consequently, it was experimentally proved that fluorescence annihilation, observable in many aryl-*o*-carborane derivatives, should occur from the C_{cage}–C_{cage} relaxed structure for the first time. Like this, because the C_{cage}–B_{cage} fused structure has no rotatable substituent groups, it can reduce some factors involved in the S_0–S_1 (or S_1–S_0) transitions. This should be desirable for the deep investigation of a PL process of aryl-*o*-carboranes.

Recently, Lee and coworkers have investigated optical properties with *o*-carborane-substituted regioisomers of aromatic hydrocarbons such as fluorene,[17] spirobifluorene,[18,22] and pyrene.[19] These reports clarified that the substitution position had a great effect on the ICT process, and different PL characters can be observed from regioisomers. The comparison with *o*-carborane-tethered anthracene isomers is another case; 1-(9-anthracenyl)-*o*-carborane[23] showed bright ICT-rich emission (Φ_{solid}: 38%), and 1-(2-anthracenyl)-*o*-carborane[24] showed relatively weaker LE-rich emission (Φ_{solid}: 8.8%). These results motivated us to investigate the relationship between the substitution position and optical properties in detail. Herein, we designed C_{cage}–B_{cage} fused isomers with the phenylnaphthalene

Department of Polymer Chemistry, Graduate School of Engineering, Kyoto University Katsura, Nishikyo-ku, Kyoto 615-8510, Japan.
E-mail: tanaka@poly.synchem.kyoto-u.ac.jp

† Electronic supplementary information (ESI) available. CCDC 2236202 and 2236203. For ESI and crystallographic data in CIF or other electronic format see DOI: https://doi.org/10.1039/d3cp00334e

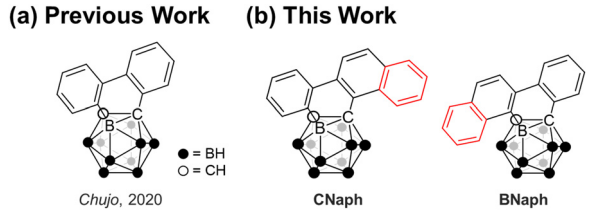

Fig. 1 The target two regioisomers obtained by a ring expansion of the previously reported carbon–boron fused *o*-carborane.[14]

ring (Fig. 1). The two isomers can be distinguished by the connecting position in the naphthalene ring: on the C_{cage} atom (**CNaph**) or the B_{cage} atom (**Bnaph**). Interestingly, optical properties were drastically varied between **CNaph** and **BNaph** despite fact that these molecules have the same chemical component as well as aromatic ring.

Results and discussion

The phenylnaphthalene-fused *o*-carboranes **CNaph** and **BNaph** were synthesized as shown in Scheme 1. The construction of the *o*-carborane scaffold was achieved by the alkyne insertion reaction with decaborane(14), and the following Pd-catalyzed intramolecular coupling reaction afforded **CNaph** and **BNaph**. Structures of the products were confirmed by ^{1}H, $^{13}C\{^{1}H\}$ and ^{11}B NMR spectroscopy, high-resolution mass spectrometory measurements and single-crystal X-ray crystallography.

From the single-crystal structural data, the ring fusing positions in **CNaph** and **BNaph** were confirmed (Fig. 2). In both compounds, the main intermolecular interaction was found to be a $C_{cage}H\cdots\pi$ interaction as often observed in many *o*-carborane derivatives.[14,25] The geometrical differences between the two isomers affected the relative arrangement of molecules; **BNaph** formed a dimer structure by mutual $C_{cage}H\cdots\pi$ interactions, and **CNaph** showed unilateral $C_{cage}H\cdots\pi$ interactions. Considering the fact that other intermolecular interactions such as a $\pi\cdots\pi$ interaction were hardly observed, the $C_{cage}H\cdots\pi$ interaction plays a significant role in determining the crystal structures.

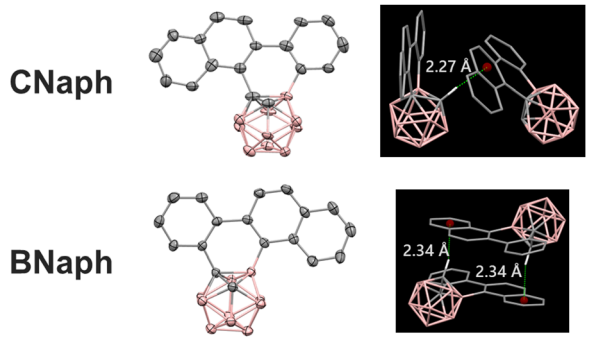

Fig. 2 Single-crystal structures of **CNaph** and **BNaph** (left) and $C_{cage}H\cdots\pi$ interactions in **CNaph** and **BNaph** (right).

UV-vis absorption spectra in $CHCl_3$ solutions were almost identical between **CNaph** and **BNaph**. The longest wavelength absorption band around 319 nm can be attributed to the π–π* transition at the phenylnaphthalene ring (Fig. 3). This fact indicates that the connecting position of the naphthalene unit has electronically little effect in the ground state. The absorption maxima of **CNaph** and **BNaph** were observed in the longer wavelength region than that of biphenyl-fused *o*-carborane (277 nm),[14,26] implying the extension of π-conjugation by the additional benzene ring.

In PL spectra, both **CNaph** and **BNaph** showed a broad structureless band around 600 nm (Fig. 3). To attribute the emission mechanism, the shift of the PL bands by changing the solvent polarity was examined. Accordingly, the peak positions were shifted to the longer wavelength region by increasing solvent polarity although the absorption peaks were inert to solvent (Fig. S1 and S2, ESI†). These results clearly indicate that the PL bands should be attributed to the ICT emission. Moreover, the ICT bands from the crystalline samples (598 nm for **CNaph** and 583 nm for **BNaph**) showed a hypsochromic shift comparing to those from the solution ones, even in non-polar methylcyclohexane solvent (599 nm for **CNaph** and 601 nm for **BNaph**). According to many reports from aryl-*o*-carboranes and our previous work in which the same trend was observed, it was

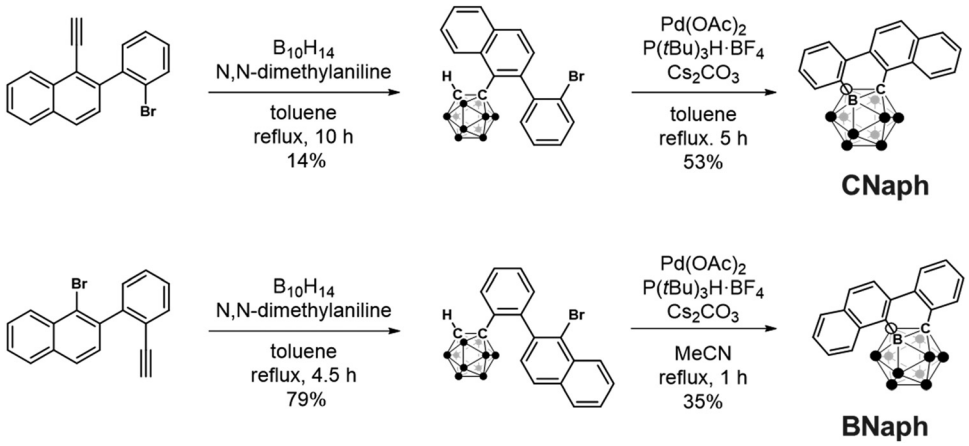

Scheme 1 Synthetic routes for **CNaph** and **BNaph**.

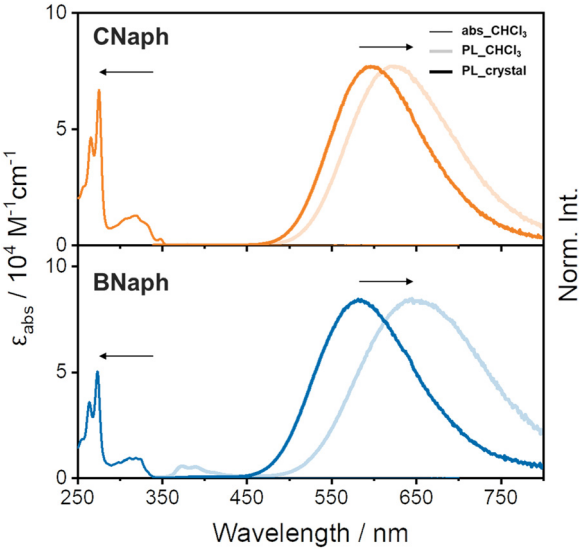

Fig. 3 Absorption (abs) and PL spectra of **CNaph** (top) and **BNaph** (bottom).

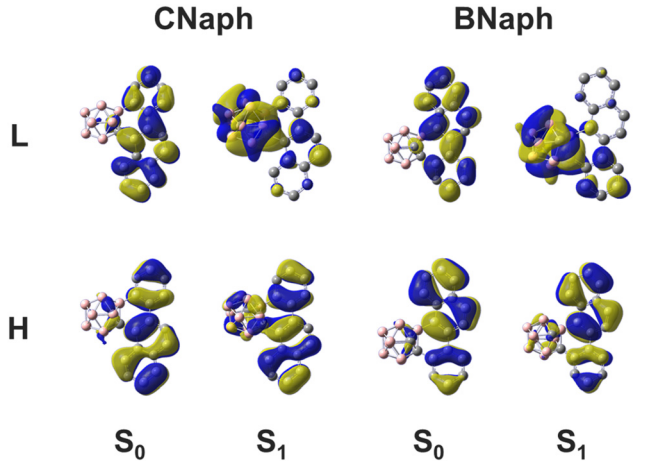

Fig. 4 Frontier orbitals of **CNaph** and **BNaph** in both S_0 and S_1 states. H and L represent HOMO and LUMO, respectively.

revealed that this spectral shift should be originated from the suppression of C_{cage}–C_{cage} elongation in the *o*-carborane unit in crystal.[14] Since structural relaxation in the excited state should be restricted in the condensed state, luminescence should be obtained from incompletely-stabilized structures. Finally, emission bands in the shorter wavelength region can be observed. Additionally, the fluorescence quantum yield was enhanced by crystallization in both compounds, indicating that these compounds have the AIE character (Table 1).[5] It is because ACQ can be avoided by suppressing intermolecular interactions owing to *o*-carborane.

Quantum chemical calculations for the isolated molecules supported the CT character (Fig. 4). In the ground state, both the highest occupied molecular orbitals (HOMOs) and the lowest unoccupied molecular orbitals (LUMOs) were on the aromatic moiety. This is the typical behavior of the locally-excited (LE) transition observed in the absorption spectra where the peak position was insensitive in solvent polarity. In contrast, LUMOs were localized mainly on the *o*-carborane unit in the S_1 excited state, indicating that *o*-carborane works as an electron-acceptor to form the ICT state. In addition, the correlation between the PL wavelength and the C_{cage}–C_{cage} elongation at the S_1 state was investigated (Table 2). In the case of the isolated molecule, the C_{cage}–C_{cage} length increased by about 0.7 Å from the S_0 to the S_1 state. On the other hand, the degree of C_{cage}–C_{cage} elongation was restricted by the surrounding molecules when the molecular coordinates of the single-crystal structure were extracted and treated by the QM/MM model (see Experimental section for detail). Although QM/MM results did not realize the qualitative tendency between **CNaph** and **BNaph**, the mechanism on the hypsochromic shift of emission bands in crystal from solution could be justified (Fig. 3). In summary, optical measurements and quantum chemical calculations showed a good correlation.

Table 1 Summary of optical properties of **CNaph** and **BNaph**

	1.0×10^{-5} M $CHCl_3$ solution				Crystal		
Compound	λ_{max}^{abs}/nm	λ_{max}^{em}/nm	τ^a/ns	$\Phi_{PL}{}^c$	λ_{max}^{em}/nm	τ^a/ns	$\Phi_{PL}{}^c$
CNaph	275/319	625	n.d.[b]	0.06	598	8.7 (7%) 15 (93%)	0.52
BNaph	274/319	374/651	n.d.[b]	0.01	583	3.1 (6%) 25 (94%)	0.32

[a] Excited at 290 nm. [b] Not determined. [c] Determined as an absolute value.

Although there were some similarities in the two regioisomers as shown above, it is notable that only **BNaph** in the solution state possessed the dual emission properties. Since the peak position of the emission band at around 374 nm was not influenced by solvent polarity, this band is attributable to LE emission (Fig. S2, ESI†). In contrast, the emssion band in the longer wavelength region is attributable to ICT emission because of the solvatochromic behavior (Fig. S2, ESI†). To gain insight on the difference in the LE/ICT balance, PL measurements in frozen glass matrices in methylcyclohexane (1.0×10^{-5} M) at 77 K were conducted (Fig. S3, ESI†). The LE emission band of **BNaph** became dominant at 77 K under the frozen condition in contrast to the ICT-rich spectra at room temperature. This result implies that there should be a significant energy barrier between the LE and ICT states.[15,23,27–29] On the other hand, the PL spectrum of **CNaph** was still dominated by ICT emission even in the frozen state, suggesting that a faint LE-ICT energy barrier should exist. These data represent that the regioisomeric ring fusing position has little effect on the electronic state of the ground state, while that has a drastic effect on the relaxation process in the excited state. On the basis of these results, the lower fluorescence quantum yield of **BNaph** than **CNaph** (Table 1) can be partially explained by quenching from the LE state as a trapping site. However, some aryl-*o*-carboranes possessing little LE/ICT barrier[30] also showed moderate Φ_{PL} values, suggesting there should be an additional

Table 2 Relationship between C_{cage}–C_{cage} bond length and PL wavelength

	One molecule			Crystal		
Compound	Calcd. C_{cage}–C_{cage}	Calcd. PL	Exp. PL	Calcd. C_{cage}–C_{cage}	Calcd. PL	Exp. PL
CNaph	S_0 : 1.65 Å S_1 : 2.43 Å	587 nm (ICT)	625 nm (ICT)[a]	S_1 : 2.31 Å[b]	485 nm[b]	598 nm
BNaph	S_0 : 1.63 Å S_1(LE) : 1.65 Å S_1(ICT) : 2.35 Å	343 nm (LE) 561 nm (ICT)	374 nm (LE)[a] 651 nm (ICT)[a]	S_1 : 2.29 Å[b]	504 nm[b]	583 nm

[a] Measured in $CHCl_3$ (1.0×10^{-5} M). [b] Estimated by QM/MM analyses.

factor relating to nonradiative decay from the ICT state to comprehend the overall PL process.[20]

Next, temperature-dependent PL spectra in $CHCl_3$ were collected for further investigation of the excited state (Fig. 5a). **CNaph** consistently exhibited only the ICT emission band, confirming the barrierless character between the LE and ICT states. The PL intensity got lower at higher temperature probably because the nonradiative decay process should be accelerated. In contrast, dual-emissive **BNaph** showed a gradual change in the LE/ICT balance. The PL spectra normalized at the LE region demonstrated the increase in the ICT emission ratio in the higher temperature region, corresponding to the assumption that there should be the significant LE/ICT energy barrier in the structural relaxation process in the excited state. Motivated by these results, we prepared the Stevens–Ban plot of **BNaph** (Fig. 5b).[31] Generally, this plot can be divided into two regions. If the LE and ICT states are in thermal equilibrium, a positive slope is obtained as eqn (1):

$$\ln\frac{I_{ICT}}{I_{LE}} = -\frac{\Delta H}{R}\frac{1}{T} + \ln\frac{k_{r,ICT}}{k_{r,LE}} \quad (1)$$

where I is fluorescence intensity, k_r is the radiative decay constant, ΔH is the enthalpy difference between LE and ICT states, and R is the gas constant. On the other hand, the nonequilibrium region between the LE and ICT states can be expressed as eqn (2):

$$\ln\frac{I_{ICT}}{I_{LE}} = -\frac{E_a}{R}\frac{1}{T} + \ln\frac{k_{r,ICT}}{k_{r,LE}} - \ln\frac{1}{\tau} \quad (2)$$

where E_a is the activation energy, and τ is the lifetime of the ICT state. Stevens–Ban plot of **BNaph** can be fitted by eqn (2) considering the nonequilibrium character. Besides, assuming that $k_{r,ICT}/k_{r,LE}$ ratio is constant over a measured temperature and τ gets shorter at the higher temperature, the lower limit of E_a can be expressed as eqn (3):

$$(\text{slope}) = -\frac{E_a}{R} + \frac{d\ln\frac{k_{r,ICT}}{k_{r,LE}}}{d\left(\frac{1}{T}\right)} - \frac{d\ln\frac{1}{\tau}}{d\left(\frac{1}{T}\right)} > -\frac{E_a}{R} \quad (3)$$

estimating that E_a should be more than 3.75 kJ mol^{-1}.

The difference in the energy barrier between **CNaph** and **BNaph** was reproduced by a quantum chemical calculation. We optimized the molecular structures both at the S_0 and S_1 states with fixing the C_{cage}–C_{cage} distance in steps of 0.1 Å. The obtained energies were plotted, indicating that only **BNaph** had the energy barrier in the S_1 state between the Franck–Condon structure and the global minimum structure (Fig. 6 and Fig. S6, ESI†). Although the scanned curve along C_{cage}–C_{cage} distance does not necessarily represent the actual relaxation pathway, the estimated E_a value 8.77 kJ mol^{-1} can be interpreted as an upper limit. This value is higher than the experimentally-obtained lower limit (3.75 kJ mol^{-1}), suggesting the true energy barrier should be between them. In addition, the plot clarified that the longer PL wavelength from **BNaph** than **CNaph** is due to the instability in S_0 energy at the S_1-optimized structure in **BNaph**.

Finally, the difference in dual-emission character is verified by considering ICT efficiency. In the ICT systems, it is generally known that the effective distance between donor and acceptor units is an important factor in determining ICT efficiency.[32]

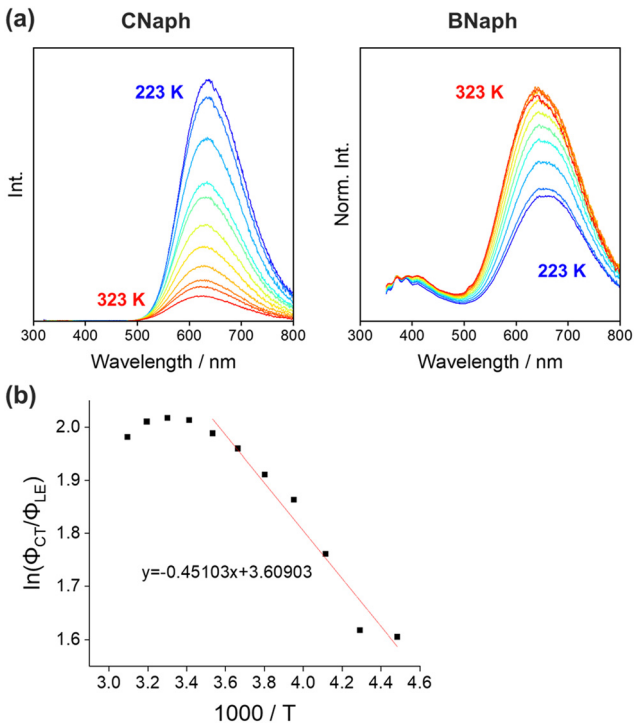

Fig. 5 (a) PL spectra of **CNaph** and **BNaph** in 1.0×10^{-5} M $CHCl_3$ solution measured at 223–323 K in steps of 10 K. (b) Stevens–Ban plot of **BNaph** in $CHCl_3$ solution and the fitting line.

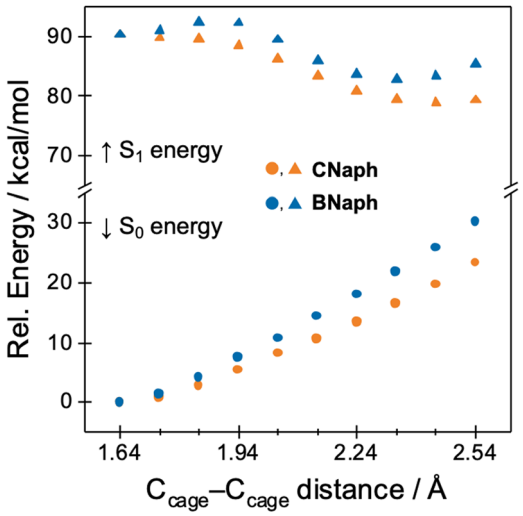

Fig. 6 Energy levels at the S_0 and S_1 states of **CNaph** (orange) and **BNaph** (blue) with variable C_{cage}–C_{cage} distance.

Considering the electron-accepting character of *o*-carborane *via* the C_{cage}–C_{cage} region and the electron-donating character of the aryl group, the relative position of the C_{cage}–C_{cage} bond and the aryl center should be critical for determining the LE/ICT balance of *o*-carboranes.[33] On the basis of this idea, we prepared the Lippert–Mataga plot to estimate the differences in the dipole moments ($\Delta\mu$) between the ground and excited states (Fig. S4, ESI†). Consequently, a greater $\Delta\mu$ value was obtained from **BNaph** (12.06 debye) than **CNaph** (8.41 debye). The more significant PL quenching of **BNaph** than **CNaph** in polar solvents (Fig. S2, ESI†) can also be attributed to the larger $\Delta\mu$ value of **BNaph**. Moreover, the natural transition orbitals (NTOs) are also consistent with the larger effective ICT distance of **BNaph** than **CNaph** (Fig. S5, ESI†). First, the distribution of electron is mainly on *o*-carborane and partially on the benzene ring connected to the C_{cage} atom in both compounds. On the other hand, the hole is distributed over a whole molecule, and the contribution of the *o*-carborane moiety is larger in **CNaph** than **BNaph**, probably because of the effective electronic communication between *o*-carborane and naphthalene than *o*-carborane and benzene.[34] Consequently, the effective distance in ICT of **CNaph** should get shorter than that of **BNaph**. These results support the experimental and computational data that showed smaller ICT efficiency in **BNaph**.

Conclusion

On the basis of the detailed investigation of the two phenylnaphthalene ring-fused regioisomers **CNaph** and **BNaph**, it is demonstrated that the substitution position of the aryl group in *o*-carborane plays a critical role in regulating the energy barrier between LE and ICT states. In particular, the temperature dependency of LE/ICT balance, the potential energy curves obtained by DFT calculation, NTO analysis, and the estimated $\Delta\mu$ values from the Lippert–Mataga plot totally supported the weakened ICT efficiency in **BNaph**. In other words, the height of the energy barrier and the dual-emission character were proved to be successfully tuned by modulating the positional relation between *o*-carborane and the aryl substituent. We believe our findings could be of significance for establishing the rational molecular design for constructing not only *o*-carborane-based emitters but also stimuli-responsive luminochromic materials.

Conflicts of interest

There are no conflicts to declare.

Acknowledgements

This work was partially supported by the Toyo Gosei Memorial Foundation and JSPS KAKENHI Grant Numbers JP21H02001 and JP21K19002 (for K.T) and JP21J14940 (for J.O).

References

1 R. N. Grimes, *Carboranes*, Elsevier, 2011.
2 W. N. Lipscomb, *Science*, 1977, **196**, 1047–1055.
3 J. Sun, M. Gao, L. Zhao, Y. Zhao, T. Li, K. Chen, X. Hu, L. He, Q. Huang, M. Liu and Y. Song, *React. Funct. Polym.*, 2022, **173**, 105213.
4 P. Stockmann, M. Gozzi, R. Kuhnert, M. B. Sárosi and E. Hey-Hawkins, *Chem. Soc. Rev.*, 2019, **48**, 3497–3512.
5 J. Ochi, K. Tanaka and Y. Chujo, *Angew. Chem., Int. Ed.*, 2020, **59**, 9841–9855 (*Angew. Chem.*, 2020, **132**, 9925–9939).
6 J. M. Oliva, N. L. Allan, P. v R. Schleyer, C. Viñas and F. Teixidor, *J. Am. Chem. Soc.*, 2005, **127**, 13538–13547.
7 J. Li, R. Pang, Z. Li, G. Lai, X. Xiao and T. Müller, *Angew. Chem., Int. Ed.*, 2019, **58**, 1397–1401 (*Angew. Chem.*, 2019, **131**, 1411–1415).
8 J. P. H. Charmant, M. F. Haddow, R. Mistry, N. C. Norman, A. G. Orpen and P. G. Pringle, *Dalton Trans.*, 2008, 1409.
9 J. Schulz, A. Kreienbrink, P. Coburger, B. Schwarze, T. Grell, P. Lönnecke and E. Hey-Hawkins, *Chem. – Eur. J.*, 2018, **24**, 6208–6216.
10 G. B. Gange, A. L. Humphries, D. E. Royzman, M. D. Smith and D. V. Peryshkov, *J. Am. Chem. Soc.*, 2021, **143**, 10842–10846.
11 M. Keener, C. Hunt, T. G. Carroll, V. Kampel, R. Dobrovetsky, T. W. Hayton and G. Ménard, *Nature*, 2020, **577**, 652–655.
12 K. Yuhara, K. Tanaka and Y. Chujo, *Mater. Chem. Front.*, 2022, **6**, 1414–1420.
13 J. Ochi, K. Yuhara, K. Tanaka and Y. Chujo, *Chem. – Eur. J.*, 2022, **28**, e202200155.
14 J. Ochi, K. Tanaka and Y. Chujo, *Dalton Trans.*, 2021, **50**, 1025–1033.
15 K. Nishino, K. Tanaka and Y. Chujo, *Asian J. Org. Chem.*, 2019, **8**, 2228–2232.
16 M. Kim, C. H. Ryu, D. K. You, J. H. Hong and K. M. Lee, *ACS Omega*, 2022, **7**, 24027–24039.

17 D. K. You, H. So, C. H. Ryu, M. Kim and K. M. Lee, *Chem. Sci.*, 2021, **12**, 8411–8423.
18 S. Kim, J. H. Lee, H. So, J. Ryu, J. Lee, H. Hwang, Y. Kim, M. H. Park and K. M. Lee, *Chem. – Eur. J.*, 2020, **26**, 548–557.
19 S. Kim, J. H. Lee, H. So, M. Kim, M. S. Mun, H. Hwang, M. H. Park and K. M. Lee, *Inorg. Chem. Front.*, 2020, **7**, 2949–2959.
20 D. Tahaoğlu, H. Usta and F. Alkan, *J. Phys. Chem. A*, 2022, **126**, 4199–4210.
21 L. Ji, S. Riese, A. Schmiedel, M. Holzapfel, M. Fest, J. Nitsch, B. F. E. Curchod, A. Friedrich, L. Wu, H. H. Al Mamari, S. Hammer, J. Pflaum, M. A. Fox, D. J. Tozer, M. Finze, C. Lambert and T. B. Marder, *Chem. Sci.*, 2022, **13**, 5205–5219.
22 S. Kim, H. So, J. H. Lee, H. Hwang, H. Kwon, M. H. Park and K. M. Lee, *Molecules*, 2019, **24**, 4135.
23 H. Naito, K. Nishino, Y. Morisaki, K. Tanaka and Y. Chujo, *Angew. Chem., Int. Ed.*, 2017, **56**, 254–259 (*Angew. Chem.*, 2017, **129**, 260–265).
24 X. Wu, J. Guo, Y. Cao, J. Zhao, W. Jia, Y. Chen and D. Jia, *Chem. Sci.*, 2018, **9**, 5270–5277.
25 R. J. Blanch, M. Williams, G. D. Fallon, M. G. Gardiner, R. Kaddour and C. L. Raston, *Angew. Chem., Int. Ed. Engl.*, 1997, **36**, 504–506.
26 Y. Morisaki, M. Tominaga, T. Ochiai and Y. Chujo, *Chem. – Asian J.*, 2014, **9**, 1247–1251.
27 K. Wada, K. Hashimoto, J. Ochi, K. Tanaka and Y. Chujo, *Aggregate*, 2021, **2**, e93.
28 H. Mori, K. Nishino, K. Wada, Y. Morisaki, K. Tanaka and Y. Chujo, *Mater. Chem. Front.*, 2018, **2**, 573–579.
29 K. Nishino, H. Yamamoto, K. Tanaka and Y. Chujo, *Org. Lett.*, 2016, **18**, 4064–4067.
30 H. Naito, K. Nishino, Y. Morisaki, K. Tanaka and Y. Chujo, *J. Mater. Chem. C*, 2017, **5**, 10047–10054.
31 U. Leinhos, W. Kuehnle and K. A. Zachariasse, *J. Phys. Chem.*, 1991, **95**, 2013–2021.
32 V. Balzani, *Electron Transfer in Chemistry*, WILEY, vol. 1, 2001.
33 K.-R. Wee, W.-S. Han, D. W. Cho, S. Kwon, C. Pac and S. O. Kang, *Angew. Chem., Int. Ed.*, 2012, **51**, 2677–2680 (*Angew. Chem.*, 2012, **124**, 2731–2734).
34 H. Naito, K. Nishino, Y. Morisaki, K. Tanaka and Y. Chujo, *Chem. – Asian J.*, 2017, **12**, 2134–2138.

